Reusable Rocket Vertical Landing

Sally Ann Keyes[1], I-Chen Su[2], and Kerry Sun[3]
University of Minnesota Twin Cities, Minneapolis, MN, 55455

The objective of this report is to demonstrate a good understanding of how to analyze nominal stability (NS), nominal performance (NP), robust stability (RS) and robust performance (RP) with designed controllers. Specifically, a mathematical LTI model was developed using data from Professor Dale Enn's DC-X rocket report. The requirements and performance specifications were set based on the objective of achieving a successful vertical landing. The open loop plant was decoupled into a SISO and SIMO system. In the SISO system, a "stable low pass" controller was based on an inner and outer loop strategy, in which the inner loop is used to control the vertical velocity. The outer loop analysis was omitted since vertical displacement control was not meaningful for the descent case. In the SIMO system, a cascaded structure was used for designing the controller. By analyzing the time response characteristics, NP was initially deemed acceptable. NS was satisfied because all the closed-loop poles, considering the nominal plant, are in the LHP. RS and RP were analyzed using single-loop-at-a-time and structured-singular value analysis (μ-analysis). NP was confirmed through this analysis as well. The RS stability properties were deemed acceptable for the SISO thrust plant, but were quite limiting for the SIMO gimbal plant. Finally, RP was NOT satisfied for either subsystem.

Nomenclature

A_x	=	Aerodynamic force on vertical coordinate
A_z	=	Aerodynamic force on vertical coordinate
b_δ	=	Gimbal actuator break frequency
b_T	=	Thrust actuator break frequency
C_x	=	Aerodynamic coefficient of lift
C_z	=	Aerodynamic coefficient of drag
C_m	=	Aerodynamic coefficient of moment
E	=	Uncertainty
E_i	=	Input uncertainty
G	=	Nominal plan transfer function
G_p	=	Plan transfer function with perturbation
g	=	Gravitational acceleration, ft/sec^2
I_{yy}	=	Moment of Inertia about y axis
L	=	Aerodynamic reference length
l_I	=	Magnitude of the relative uncertainty
m	=	Mass of rocket, slug
m_y	=	Aerodynamic moment about y axis
$\bar{q}$	=	Dynamic pressure
T	=	Thrust force, lb
T_{max}	=	Maximum thrust
T_{min}	=	Minimum thrust
$\dot{T}_{max}$	=	Maximum thrust rate
x	=	Vertical coordinate, ft

American Institute of Aeronautics and Astronautics

$\dot{x}$	=	Vertical velocity , ft/s
x_a	=	Vertical wind force
w_p	=	Performance weight
w_I	=	Multiplicative Uncertainty Weighting
z	=	Horizontal coordinate, ft
$\dot{z}$	=	Horizontal velocity, ft/s
z_a	=	Horizontal wind force
α	=	Angle of attack
ρ	=	Air density
μ	=	Structure Singular Value
θ	=	Pitch rotation angle
$\dot{\theta}$	=	Pitch rotation rate
δ	=	Vehicle center line through angle
δ_{max}	=	Maximum gimbal angle
$\dot{\delta}_{max}$	=	Maximum gimbal rate, rad/s
Δ	=	Perturbation

I. Project Definition

The project studied and analyzed vertical landing of a rocket. Specifically, nominal stability (NS), nominal performance (NP), robust stability (RS) and robust performance (RP) were analyzed with designed controllers. The numerical values in the model were based on the DC-X, a vertical landing and take off vehicle. The mathematical model of the rocket was verified and numerical data was obtained from the document "Guidance & Control For DC-X Hover & Translate Flights," by Professor Dale Enns. The report illustrates the process of controller design. In section II, the transfer function of open loop is derived from the physical and mathematical model. In section III and IV, the desired requirement is defined. The strategy to design the controller is shown in section V. After the controller is designed, the nominal stability, nominal performance, robust stability and robust performance is analyzed in section VI, VII, VIII, IX respectively.

II. Mathematical Model

The rocket model will only consider vertical planar motion of a rigid body. This is shown in Figure 1 (Enns). Cartesian coordinates were used for this problem. The vertical coordinate is x, the horizontal coordinate is z and the pitch rotation is θ. The thrust force is T, which is gimbaled relative to the vehicle centerline though the angle δ. The aerodynamic forces and moments are A_x, A_y, and m_y respectively as also shown in Figure 1 (Enns).
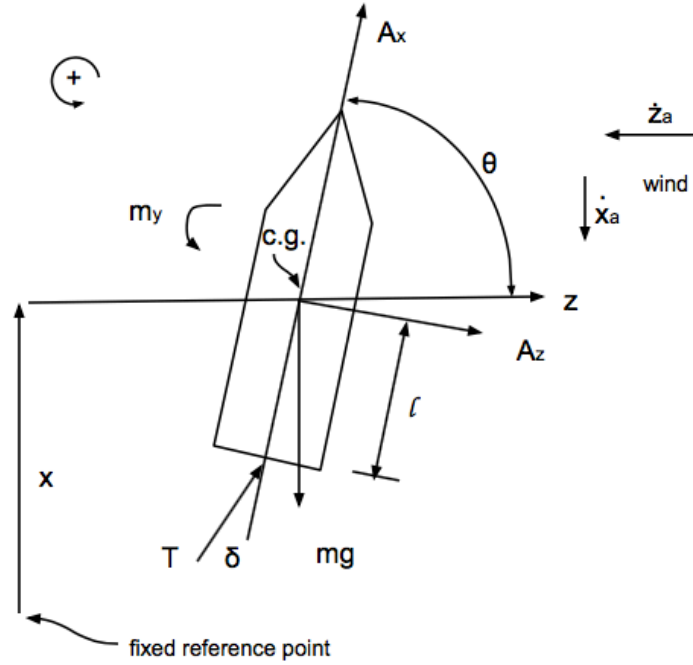
Figure 1. Vehicle Definition.

Three ordinary nonlinear differential equations were developed (Enns) using the Newton-Euler equations, as shown in eq. (1), (2) and (3):

$$m\ddot{x} = T\sin(\theta - \delta) - mg - A_z \cos(\theta) + A_x \sin(\theta) \tag{1}$$

$$m\ddot{z} = T\cos(\theta - \delta) + A_z \sin(\theta) + A_x \cos(\theta) \tag{2}$$

$$I_{yy}\ddot{\theta} = Tl\sin(\delta) + m_y \tag{3}$$

where I_{yy} is the moment of inertia, and l is the effective moment arm between the center of mass and the engines. The aerodynamic forces and moments are given by eq. (4), (5) and (6):

$$A_x = \bar{q}SC_x(\alpha) \tag{4}$$

$$A_z = \bar{q}SC_z(\alpha) \tag{5}$$

$$m_y = \bar{q}SL\left\{C_m(\alpha) + C_{m_q} \frac{L\dot{\theta}}{2\sqrt{(\dot{x} + \dot{x}_a)^2 + (\dot{z} + \dot{z}_a)^2}}\right\} \tag{6}$$

where S is the aerodynamic reference area, L is the aerodynamic reference length, $\bar{q}$ is the dynamic pressure and α is the angle-of-attack, C_{m_q} = -0.5 (Enns), and the 3 aerodynamic coefficients are plotted in Figure 2, Figure 3, and Figure 4 (Enns).

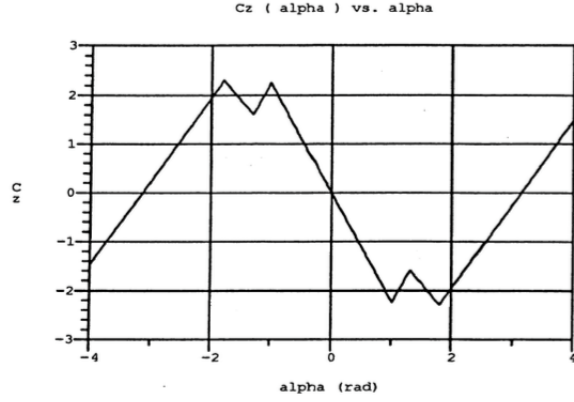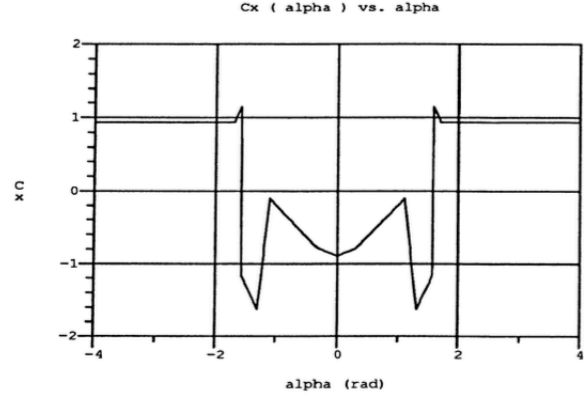**Figure 2. Coefficient of Drag vs. Angle-of-Attack.**

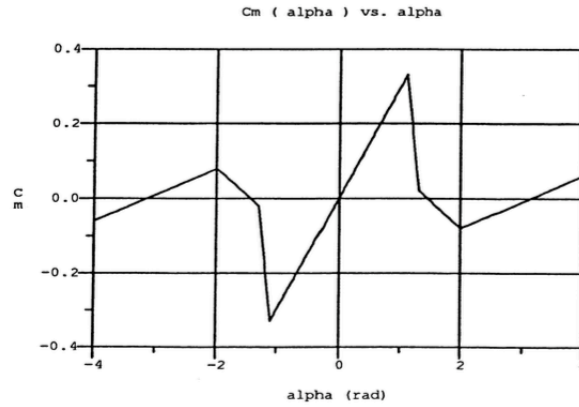**Figure 3. Coefficient of Lift vs. Angle-of-Attack.**

Figure 4. Coefficient of Moment vs. Angle-of-Attack.

The dynamic pressure and angle-of-attack depend on the atmospheric motion as well as the vehicle velocity shown in eq. (7) , (8), and (9):

$$\bar{q} = \frac{1}{2}\rho[(\dot{x} + \dot{x}_a)^2 + (\dot{z} + \dot{z}_a)^2] \tag{7}$$

$$\alpha_{up} = \theta - \tan^{-1}\left(\frac{\dot{x} + \dot{x}_a}{\dot{z} + \dot{z}_a}\right) \tag{8}$$

$$\alpha_{down} = \theta + \pi - \tan^{-1}\left(\frac{\dot{x} + \dot{x}_a}{\dot{z} + \dot{z}_a}\right) \tag{9}$$

where ρ is the air density (which depends on altitude), and $\dot{x}_a > 0$ a vertical wind from above and $\dot{z}_a > 0$ is a horizontal wind from the right as seen in Figure 1. Note that the equation for the angle of attack includes an addition term π when the velocity is negative and the rocket is descending.

Vertical descent case is analyzed in this study. The equilibrium condition is achieved where there is no wind, and $\delta = \delta_0 = 0, \theta = \theta_0 = \frac{\pi}{2}, A_x = A_{x_o}, A_z = A_{z_o} = 0, m_y = m_{y_o} = 0$ and $T = T_o = mg - A_{x_o}$. Linearized equations and associated transfer functions were derived for descent case with numerical data given in Table 1.

The data contained in Table 1 was used for numerical evaluation. For the numerical transfer functions and state space representation to be presented, x and z in ft, θ and δ are in radians, and T is in lbs. The altitude was assumed to be 5,000 ft. The standard atmosphere air density at 5,000 ft altitude was used for the numerical evaluation of the transfer functions and state space representation. The descent rate was $\dot{x} = -300$ ft/sec (Enns) with zero wind.

Table 1. Vehicle Numerical Data

Variable	Symbol	Value	Unit
weight	mg	321,170	lbs
inertia	I_{yy}	117,950	slugs-ft^2
moment arm	l	13.6	ft
ref. area	S	169.47	ft^2
ref. length	L	39.663	ft
max. gimbal	δ_{max}	0.14	radians
max. gimbal rate	$\dot{\delta}_{max}$	0.5236	rad/sec
gimbal actuator break freq.	b_{δ}	30	rad/sec
min. thrust	T_{min}	13,200	lbs
max. thrust	T_{max}	55,200	lbs
max. thrust rate	$\dot{T}_{max}$	36,772	lbs/sec
thrust actuator break freq.	b_T	5.34	rad/sec
Coefficient of lift	$C_z\|_{\alpha=\pi}$	0	
Coefficient of drag	$C_x\|_{\alpha=\pi}$	0.7	
Coefficient of moment	$C_m\|_{\alpha=\pi}$	0	
Coefficient of pitch damping moment	C_{mq}	-0.5	
Lift Curve Slope (nose aft)	$\frac{dC_z}{d\alpha}\|_{\alpha=\pi}$	1.71	1/rad
Drag Curve Slope (nose aft)	$\frac{dC_x}{d\alpha}\|_{\alpha=\pi}$	0	1/rad
Moment Curve Slope (nose aft)	$\frac{dC_m}{d\alpha}\|_{\alpha=\pi}$	0.0701	1/rad

The 3 nonlinear differential equations were linearized about the descent equilibrium condition and they were represented in Linear Time Invariant (LTI) state space form as shown in eq. (10). Appendix C contains information on how the equations were linearized and put into state space form. The variable x contains 6 states, they are vertical displacement (x), horizontal displacement (z), pitch rotation angle (θ), vertical velocity ($\dot{x}$), horizontal velocity ($\dot{z}$), and pitch rate ($\dot{\theta}$) as shown in eq. (11). The variable u contains 2 inputs as shown in eq. (12), they are thrust force T and gimbaled angle δ. The outputs include all the 6 states. The state space equations calculated represent perturbations from the trim condition, as is emphasized in eq. (11) Here the symbol δ represents an incremental change in the state and input values, rather than the gimbal angle. After this point, the symbol δ will be replaced by a subscript 1, indicating the perturbed state.

$$\delta\dot{x} = A\delta x + B\delta u$$
$$\delta y = C\delta x + D\delta u \tag{10}$$

$$x = \begin{bmatrix} x \\ z \\ \theta \\ \dot{x} \\ \dot{z} \\ \dot{\theta} \end{bmatrix} \tag{11}$$

$$u = \begin{bmatrix} T \\ \delta \end{bmatrix} \tag{12}$$

The corresponding A, B, C, D, matrices were represented in Eq. (13), (14), (15), and (16). The rank of the controllability matrix of the system is 6 (equal to the number of states), confirming that the problem is well posed and there exists a controller for the rocket. C is an identity matrix because it is assumed that all the states are observed by sensors whose outputs are exactly the state values. D is assumed to be a zero matrix for simplicity.

$$A = \begin{bmatrix} 0 & 0 & 0 & 1 & 0 & 0 \\ 0 & 0 & 0 & 0 & 1 & 0 \\ 0 & 0 & 0 & 0 & 0 & 1 \\ 0 & 0 & 0 & -0.07295 & 0 & 0 \\ 0 & 0 & -5.468 & 0 & -0.08911 & 0 \\ 0 & 0 & 0.3682 & 0 & -0.001227 & -0.1736 \end{bmatrix} \tag{13}$$

$$B = \begin{bmatrix} 0 & 0 \\ 0 & 0 \\ 0 & 0 \\ 0.001001 & 0 \\ 0 & 21.26 \\ 0 & 2.449 \end{bmatrix} \tag{14}$$

$$C = \begin{bmatrix} 1 & 0 & 0 & 0 & 0 & 0 \\ 0 & 1 & 0 & 0 & 0 & 0 \\ 0 & 0 & 1 & 0 & 0 & 0 \\ 0 & 0 & 0 & 1 & 0 & 0 \\ 0 & 0 & 0 & 0 & 1 & 0 \\ 0 & 0 & 0 & 0 & 0 & 1 \end{bmatrix} \tag{15}$$

$$D = \begin{bmatrix} 0 & 0 \\ 0 & 0 \\ 0 & 0 \\ 0 & 0 \\ 0 & 0 \\ 0 & 0 \end{bmatrix} \tag{16}$$

The associated transfer functions were also derived and given in Eq. (16), (17) and (18). Note that the aerodynamics couples the horizontal and rotational degrees of freedom. The unstable pole in Eq. (18) and (19) corresponds to the aerodynamic instability and the two stable poles are a result of the negative $\dot{x}_o$. The stable pole in Eq. (17) corresponds to drag damping. The other marginally stable pole in the vertical transfer function arises because the derivative of air density with respect to altitude was assumed to be negligible. If included, that derivative will give rise to a stable real pole that is only slightly offset from the origin. Furthermore, the vertical displacement transfer function is minimum phase, although the horizontal displacement and the rotational transfer functions are non-minimum phase.

$$\frac{x_1(s)}{T_1(s)} = \frac{0.001001}{s(s + 0.07295)} \tag{17}$$

$$\frac{z_1(s)}{\delta_1(s)} = \frac{21.26(s - 0.915804)(s + 1.08937)}{s(s - 0.534864)(s + 0.106996)(s + 0.690568)} \tag{18}$$

$$\frac{\theta_1(s)}{\delta_1(s)} = \frac{2.449(s + 0.07845)}{s(s - 0.534864)(s + 0.106996)(s + 0.690568)} \tag{19}$$

Disturbances were also considered for analysis. The disturbances considered are wind, a change in mass, and a change in the moment of inertia. Matrix B_d was created, similar to the matrix B, to consider the effects of possible disturbances. It was found that only disturbances due to wind had significant effects, and the problem statement deals only with horizontal wind. The following state space matrix, B_d, represents the input of horizontal wind, shown in Eq. (20). The resulting transfer functions are calculated, and only the horizontal displacement and the rotation are affected, as seen in Eq. (21) and (22). Note that the state space matrices A, C, and D are unchanged and are therefore not repeated here. Horizontal wind is denoted $\dot{z}_a$.

$$B_d = \begin{bmatrix} 0 \\ 0 \\ 0 \\ 0 \\ -0.0891 \\ -0.0012 \end{bmatrix} \tag{20}$$

$$\frac{z_1(s)}{\dot{z}_a(s)} = \frac{-0.0891(s - 0.5848)(s + 0.7584)}{s(s - 0.5349)(s + 0.1067)(s + 0.6906)} \tag{21}$$

$$\frac{\theta_1(s)}{\dot{z}_a(s)} = \frac{-0.0012s}{(s - 0.5349)(s + 0.1067)(s + 0.6906)} \tag{22}$$

Table 2 lists all the corresponding open loop system poles and Table 3 lists all the corresponding open loop system zeros. Note that the right half plane open loop zero is very close in magnitude to the unstable pole in the horizontal displacement transfer function (Eq. (18): approximately 1 and 0.5, respectively). This causes challenges when controlling the system, which will be addressed in the later section.

Table 2. Poles of Open Loop System

	Open loop poles
$\dfrac{z_1(s)}{\delta_1(s)}$ or $\dfrac{\theta_1(s)}{\delta_1(s)}$	0
	-0.6908
	-0.1066
	0.5347
$\dfrac{x_1(s)}{T_1(s)}$	-0.0730

Table 3. Zeros of Open Loop System

	Open loop zeros
$\dfrac{z_1(s)}{\delta_1(s)}$	0.9158
	-1.0894
$\dfrac{\theta_1(s)}{\delta_1(s)}$	-0.0784

Notice the plant can be decoupled into 2 sub-plants and each sub-plant is only controlled by one input. Specifically, The vertical displacement (x) and vertical velocity ($\dot{x}$) are only controlled by thrust force $\boldsymbol{T}$. Also, the horizontal displacement (z), pitch rotation angle ($\boldsymbol{\theta}$), horizontal velocity ($\dot{\boldsymbol{z}}$), and pitch rate ($\dot{\boldsymbol{\theta}}$) are only controlled by gimbaled angle $\boldsymbol{\delta}$. This unique characteristic of the plant will be exploited when designing the control law. The 2 sub-plants therefore will be controlled separately.

Also, it was commented that the rocket is not unstable because of the negative $\dot{x}$ and is unstable for positive $\dot{x}$ also. The instability has to do with the cubic open loop characteristic equation not including the pole at the origin. The aerodynamic moment due to $\dot{z}$, makes a hovering vehicle unstable independent of where the cg is located. This is a flight vehicle modeling topic and beyond the scope of EE 5235. The open loop poles are approximately the 3 cube roots of a positive or negative real number.

III.   Design Requirements

The requirements for the design were also partly based the DC-X vehicle report. The major requirements such as stability and trajectory tracking were considered.

Both nominal and robust stability were required for the project. Nominal Stability requires that closed-loop eigenvalues (associated with linearization of the nominal closed-loop vehicle and control law models) lie in the left half plane (LHP). Robust stability requires the closed-loop system possess adequate stability margins. Stability margins include gain and phase margins. Also, structured singular value was used for robust stability.

The critical tracking requirements are to land within 100 ft in the horizontal direction (Enns), and vertical and horizontal velocities less than 3.5 ft/sec and 5 ft/sec (Enns), respectively. Furthermore, the rocket should be within 2 degrees of the vertical orientation at landing (Enns). This should be achieved under the presence of steady winds of 12 knots near ground (20.25 ft/s), and increasing to 35 knots (59.01 ft/s) at 6000 m altitude (Enns).

IV.   Performance Specification

A. Time-Domain Performance Specifications

Rise time, settling time, percent overshoot and steady-state error should all be considered. For the given system, the rise time and settling time should be small. The percent overshoot should be less than 10%, corresponding to a damping ratio of approximately 0.6 for second order systems. Steady-state errors depend on both the system and the input command or disturbance. Steady-state errors should be near zero, although nonzero errors are always present because of non-linearities, measurement uncertainties, and disturbances in the system. As such, the steady state error is restricted to 5%. The transfer function from thrust to vertical position is already stable and of type 1 (one pole at the origin), indicating that in unity feedback it should track a step input without error and a ramp input with a finite error.

B. Frequency-Domain Performance Specifications

For the final system, a satisfactory controller should yield the following: a stable closed-loop system, good tracking, good disturbance rejection, tracking and stability robustness in the presence of modeling errors, and sensor noise rejection. Specifically, all the open loop transfer functions should have at least +-6 dB gain margin (GM) and 45 to 60 degrees of phase margin (PM). The sensitivity function S should be small (S <<1) at low frequencies for good reference tracking and disturbance rejection. Also, small complementary sensitivity function T (T <<1) should be achieved for noise rejection at high frequencies. The specifications are relative to the crossover frequencies for the closed-loop transfer functions, which will be based on the break frequencies of the gimbal and thrust actuator (30 rad/s and 5.3 rad/s respectively). There should be a smooth transition from low to high frequency, with a slope greater than -30 dB/decade near the gain crossover frequency for robustness.

Furthermore, in order to check the nominal performance of the system, Eq. (23) should be satisfied. For nominal performance (NP), the maximum amplitude of S should be bounded by $\left|1/w_{P(s)}\right|$ where $w_{P(s)}$ is the weight function for a particular sensitivity function. The strategy for selecting the weight function is shown in Eq. (24). This weight representation was taken from "Multivariable Feedback Control" by Skogestad on page 60[2]. M is the maximum amplitude of the sensitivity function, $w^{*}{}_{B}$ is the minimum bandwidth frequency of S, A is the maximum steady state tracking error and n is integer for shaping the weight function. For robust performance (RP), Eq. (25) has to be satisfied with appropriate weightings, where the weighting used for this project takes the form shown in Eq. (26). This is a simple multiplicative weighting that represents unmodeled dynamics uncertainty. In this form r_0 is the

relative uncertainty at steady state, $1/\tau$ is approximately the frequency at which the relative uncertainty reaches 100%, and r_∞ is the magnitude of the weight at high frequency.

$$\| w_P S \|_\infty < 1 \text{ for all frequencies} \tag{23}$$

$$w_P(s) = \left(\frac{\frac{s}{M^{1/n}} + w^*_B}{s + w^*_B A^{1/n}} \right)^n \tag{24}$$

$$\| w_I T \|_\infty + \| w_P S \|_\infty < 1 \text{ for all frequencies} \tag{25}$$

$$w_I(s) = \frac{\tau s + r_0}{(\tau/r_\infty)s + 1} \tag{26}$$

V. Controller Design

1. Thruster Control

Looking at the first sub-plant (from input thrust force T to the vertical displacement x and vertical velocity $\dot{x}$), and eq. (17), an inner-outer loop strategy was implemented due to plant's structure. The inner loop relates thrust T to $\dot{x}$, this is shown in Figure 5.

A "stable low pass" controller will be implemented to control the inner loop first. From thrust T to $\dot{x}$, this is a 1st order stable transfer function given in Eq. (27). The stable low pass form is given in Eq. (28). The selected closed-loop frequency was set to be 5.34 rad/s to match the thrust actuator break frequency listed in Table 1 (note that this was commented to be large, and it could result a small damping ratio). The open loop transfer function and the closed inner loop were calculated in Eq. (29) and (30). The closed inner loop was stable (stable low pass). Based on the time domain specification and the limitation of physical rocket, overshoot should be controlled to be less than 5% for the inner loop because the limitation on rocket final touchdown velocity. The setting time can be 2 to 3 minutes, which seems to be long for landing. Perhaps a better controller should be designed in the future.

The outer loop was omitted for descending analysis because it was not meaningful to control the position if the rocket is not hovering. The position would decrease because it's descending, and velocity would be the main interest for analysis. Hence the outer loop was not analyzed.

$$G_1 = (sI + P)^{-1}H = \frac{0.001}{s + 0.073} \tag{27}$$

$$K_1 = H^{-1}(I + \frac{1}{s}P)\Omega_c = \frac{5340s + 389.8}{s} \tag{28}$$

$$L_1 = G_1 K_1 = \frac{1}{s}\Omega_c = \frac{5.34}{s} \tag{29}$$

$$\frac{\dot{x}(s)}{T_{cmd}(s)} = T_1 = (1 + L_1)^{-1}L_1 = \frac{5.34}{s + 5.34} \tag{30}$$

The Simulink block diagram for thruster was shown in Figure 5 below. The inner loop structure can be seen clearly. The inner-loop with "stable low pass" controls vertical velocity. All the grey tabs were used for analyzing RS and RP at later sections. All the weighting transfer functions were shown in blue (w_I), orange (w_p) and green block (w_s) for RS and RP analysis as well.
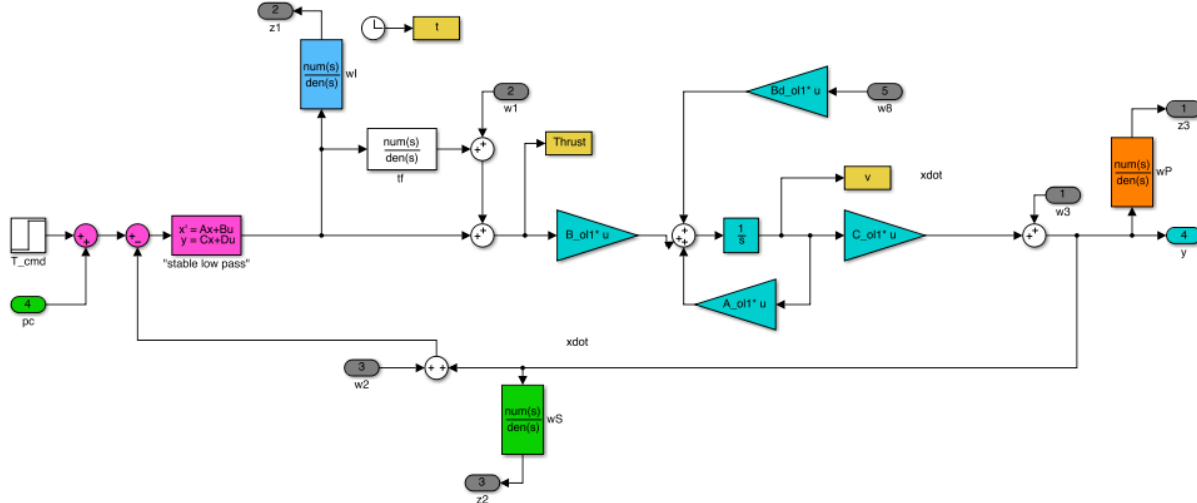

Figure 5. Inner Loop Thruster Control: Thrust to $\dot{x}$.

2. Gimbal Angle Control

For the linearization condition, the horizontal position (z) and the angular orientation (θ) are only affected by the gimbaled angle (δ). Furthermore, it can be shown that the relationship between the states may be approximated by a chain of integrators. The approximate relationships are shown in Eq. (31) to (36), which are derived using small angle approximations, setting thrust equal to gravitational force, and neglecting certain dynamics such as aerodynamic effects. Eq. (31) and (32) describe the dynamics and Eq. (33) to (36) show the integrator relationship in the Laplace domain.

$$\ddot{\theta} \approx \frac{mgl}{I_{yy}}\delta \qquad (31)$$

$$\ddot{z} \approx -g\theta \qquad (32)$$

$$\dot{\theta} \approx \frac{1}{s}\frac{mgl}{I_{yy}}\delta \qquad (33)$$

$$\theta \approx \frac{1}{s}\dot{\theta} \qquad (34)$$

$$\dot{z} \approx \frac{1}{s}(-g)\theta \qquad (35)$$

$$z \approx \frac{1}{s}\dot{z} \qquad (36)$$

Exploiting this relationship, a cascaded structure was used for the controller architecture. This structure is shown in Figure 6. The structure consists of four loops, where each loop is designed to shape a specific entry of the transfer

function. The reduced plant is a 4x1 transfer function matrix, and the loops are created using feedback of individual outputs. From inner to outer loop, the elements used in feedback are $\dot{\theta}, \theta, \dot{z}$, and z, corresponding to transfer function entries 4 through 1.

Because of the integrator relationship shown in Eq. (31) through (36), each loop is shaped by simply setting the cross over frequency of the matrix entry of interest (the fourth entry for the first loop). This follows standard procedure for loop shaping when dealing with plants that are integrators. As a starting point, the gains necessary to create the desired crossover frequencies could be estimated by the relationships in Eq. (31) through (36). In order to be more precise, however, the gains were selected analytically by evaluating the full model, rather than just the approximate integrator. Given a desired crossover frequency, the transfer function magnitude at that frequency was calculated and set to be the inverse of the necessary gain. In this way, the loops is shifted either up or down by an amount that ensures the final loop gain at the desired crossover frequency will be equal to one.

Working from the inner feedback loop to the outer, each gain is selected and the loop is then closed by feeding back the output of the transfer function of interest (in Simulink, this is done by multiplying the output by a matrix H_i that returns on the output of interest, shown in Figure 6). The next loop is designed in a similar way, treating the recently closed loop as the new plant and selecting a gain to set the crossover frequency of the new open loop. Furthermore, each gain and loop closure will affect each entry of the transfer function, even though only one entry is used to select the a given gain. Therefore, it is important to sequentially select a gain and close the corresponding loop before designing the following loop. As a result, every loop accounts for each of the nested loops within it, but is designed independently of the loops outside of it.

As a rule of thumb, each crossover frequency should be less than the crossover frequency of the loop inside of it (typically by over a factor of 2). Eq. (37) was used to calculate the loop gains and is shown below, where G_i is the $(5-i)^{th}$ element of the ith closed loop transfer function (the first closed loop transfer function being simply the plant).

$$gain_i = \frac{1}{|G_i(jw_{c_i})|} \tag{37}$$

Once the loop structure was implemented, the crossover frequencies were carefully selected and tuned to achieve optimal performance. The inner loop, also the fastest loop, was assigned a crossover frequency of 5. This was selected because it is sufficiently fast compared to the unstable pole at 0.53 but still sufficiently slow compared to the break frequency of the gimbal actuator at 30 rad/s. The crossover frequency of the second loop was 0.36 times frequency for the final two loops was slightly more complicated because the z dynamics introduced a negative gain and a zero in the right half plane at 0.92. The nearness of the pole and zero in the right half plane made it difficult to achieve stability as well as satisfactory performance. Typically, the loop should be two to three times faster than a right half plane pole as well as two to three times faster than a right half plane zero. This is impossible for the given plant, where the pole and zero are separated by less than a factor of two.

The crossover frequency of the third loop was reduced from the second loop by a factor of approximately 5. This was intended to add additional separation between the θ and z dynamics and reduce unwanted coupling. Additionally, the gain for the third loop was made negative in order to account for the negative gain in the dynamics, corresponding to a position change in rocket rotation to a negative change in horizontal displacement. The crossover frequency for the fourth and final loop was selected by first reducing the third loop crossover frequency by a factor of 2, and then tuning it in order to achieve a satisfactory response. Ultimately, a crossover frequency was chosen that does not satisfy the general rule of decreasing by a factor of 2, but this frequency seemed to give the best time domain response. Table 3 shows the final crossover frequencies and related gains for the 4 cascaded open loops. It is important to note that the gains in Table 3 are absolute, and any of the pertinent variables listed in Eq. (31) through (36) (such as m, g, l, and I_{yy}) are embedded in these numbers.

Table 4. Cascaded Controller: Gains of each closed loop

	$\dot{\theta}$ feedback loop	θ feedback loop	$\dot{z}$ feedback loop	z feedback loop
Crossover Frequency (w_c)	5 rad/s	1.8 rad/s	0.35 rad/s	0.2 rad/s
Gain (Kp)	2.0733	1.9971	-0.0357	0.2613

The outermost closed loop transfer functions were obtained for z, $\dot{z}$, θ and $\dot{\theta}$ in Eq. (38) to (41) shown below. All the poles of the resulting transfer functions are located in the LHP, which implies the all of channels of the final closed loop are stable.

$$\frac{z(s)}{z_{cmd}(s)} = \frac{-0.8206\,(s+1.09)(s-0.916)}{(s^2+0.4501\,s+0.1033)(s^2+1.749s+7.929)} \tag{38}$$

$$\frac{\dot{z}(s)}{z_{cmd}(s)} = \frac{-0.8206\,s(s+1.09)(s-0.916)}{(s^2+0.4501\,s+0.1033)(s^2+1.749s+7.929)} \tag{39}$$

$$\frac{\theta(s)}{z_{cmd}(s)} = \frac{-0.094524s(s+0.07868)}{(s^2+0.4501\,s+0.1033)(s^2+1.749s+7.929)} \tag{40}$$

$$\frac{\dot{\theta}(s)}{z_{cmd}(s)} = \frac{-0.094524s^2(s+0.07868)}{(s^2+0.4501\,s+0.1033)(s^2+1.749s+7.929)} \tag{41}$$

The end result of this controller structure is that one reference command (horizontal position) dictates the behavior of the four described outputs. Essentially, the outer loops that control z determine what θ is necessary to achieve the desired reference. The inner loops then determine what δ is necessary to achieve the desired θ. For a constant reference command, each of the inner loops is eventually driven to zero, stabilizing the rotation and horizontal velocity of the rocket. Although this only allows for direct control of horizontal position, this is desirable for the rocket application, where these output perturbations should be equal to zero for an optimal landing.

The Simulink block diagram for gimbal was shown in Figure 6 below. A cascaded control design was implemented. All the grey tabs were used for analyzing RS and RP at later sections. All the weighting transfer functions were shown in blue (w_I), orange (w_p) and green block (w_s) for RS and RP analysis as well.
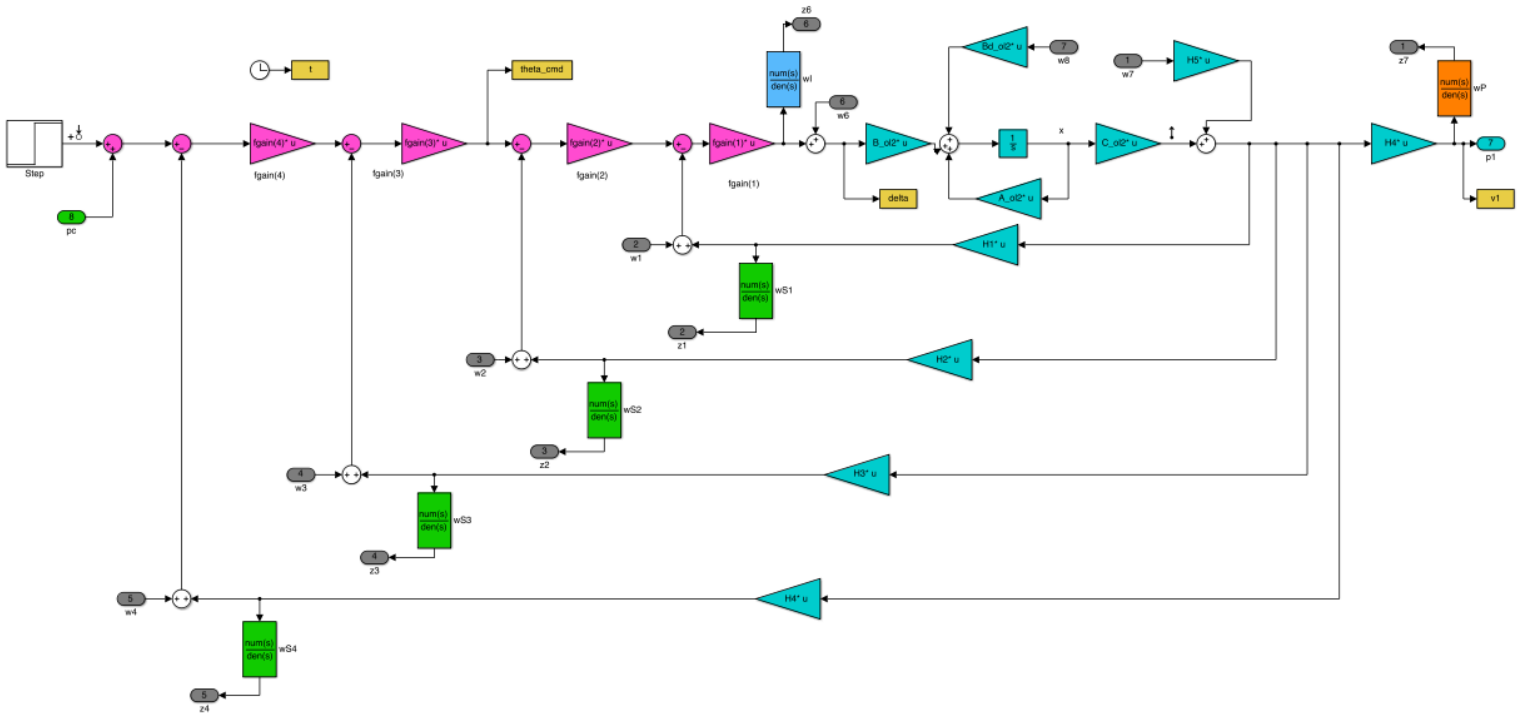
Figure 6. Simulink Block Diagram for Gimbal Angle control.

VI.   Nominal Performance

1. Thruster Control Simulation & Performance

Using Matlab Simulink, both step responses and Bode diagrams were plotted. Figure 7 was the unit step response of the inner closed loop for vertical velocity. The initial response was quite fast. This fast response was due to designed crossover frequency 5.34 rad/s. The rise time for vertical velocity was about 0.4 seconds, and settling time was about 1 second. There was no overshoot and steady state error the vertical velocity. The "stable low pass" controller hence looked reasonable.
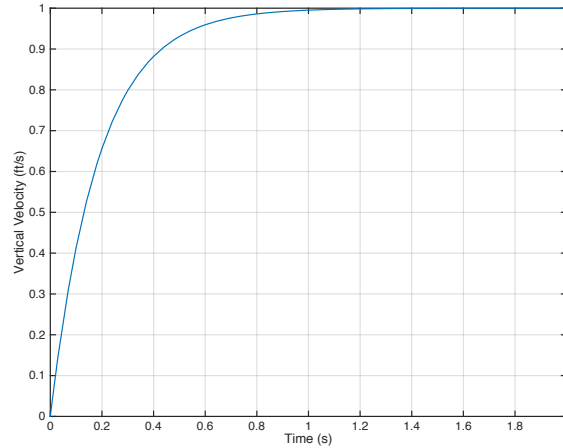
Figure 7. Step Response for Inner loop Vertical Velocity.

Figure 8 showed thruster input versus time. The maximum thrust was about 6000 lbs. Adding this to the trim condition (32,000 lbs), the maximum thrust was about 38,000 lbs. This is acceptable given in specification (55,200 lbs). Figure 9 showed thrust input rate versus time. The maximum thrust rate was about 30,000 lbs/sec. Note that this is only the response to a 1ft/sec change in velocity. If 10 ft/s was needed, the upper limit would be broken. In that case, a new controller is needed. This was below maximum thrust rate (36,772 lbs). The thrust response hence looked reasonable.
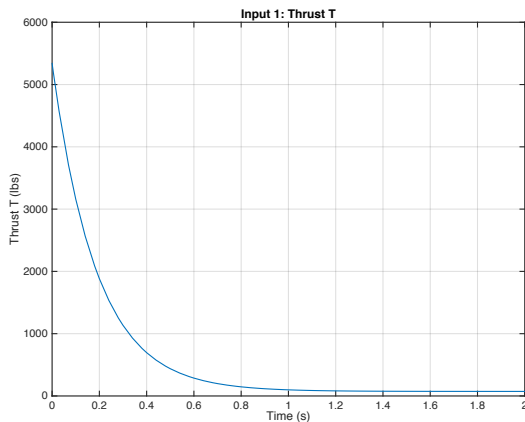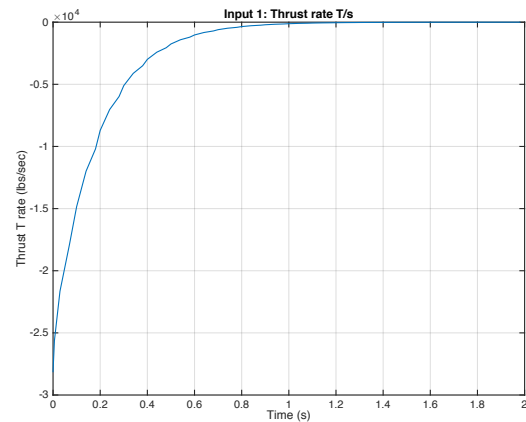
Figure 8. Input Thrust T vs. Time.   **Figure 9. Input Thrust Rate vs. Time.**

2. Gimbal Control Simulation & Performance

Figure 10 to 13 showed the step response of horizontal displacement, horizontal velocity, pitch rotation angle and pitch rotation rate. Looking at Figure 10, the rise time was 13.5 seconds and its peak value was 1.05. The overshoot was 5.14%, which is a tolerable. The settling time was around 23 second and there was no steady-state error in the step response. Notice the horizontal displacement undershoot due to a positive, or RHP, zero in Eq. (38). In Figure 11, the step response of horizontal velocity also has a negative overshoot for the same reason. The undershoot is quickly followed by an overshoot of about 0.22 ft/s in 1 second. Although somewhat abrupt, this change (0.35 ft/s) in velocity was deemed to be acceptable and difficult to avoid due to the underlying plant dynamics. After approximately 25 seconds, the response reached a steady state value of zero. The horizontal velocity should be zero as expected because the rocket should have minimal horizontal velocity while landing. Drifting away from the designed location should also be minimized, and therefor the horizontal position should approach zero at steady state, which it does. In Figure 12, the pitch rotation angle firstly undershot to -0.7 degrees, and then went back up to 0.1 deg. it reached zero within 20 seconds. Figure 13 showed the pitch rotation rate has a underdamping effect. This effect was related to the closed loop set of poles with 0.31 damping ratio. This effect quickly died out after about 8 seconds. The settling time of all of the step response were reasonable, which means the controller was sufficient enough to control the rocket before touchdown.

Figure 14 and 15 showed the gimbal angle and gimbal angle rate versus time. The maximum gimbal angle was 2 degrees, which is lower than the specification value 8.012 degrees (0.14 rad). The maximum gimbal angle rate was 0.09 degrees/s, which is also lower than the specification value 30 degrees/s (0.5236 rad/s). Therefore, the controller for the gimbal angle and gimbal angle rate is practical. Note again this was for 1 degree/sec gimbal command. If a large step command was needed, the controller probably has to be redesigned.
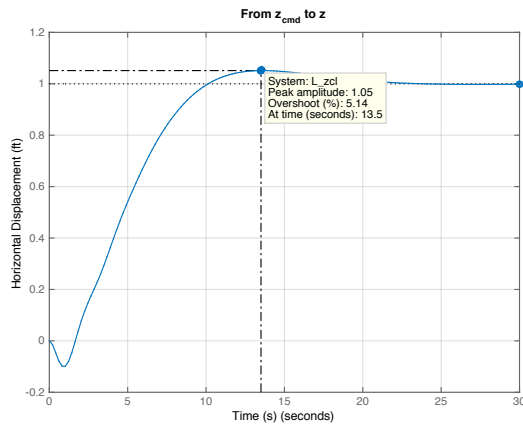

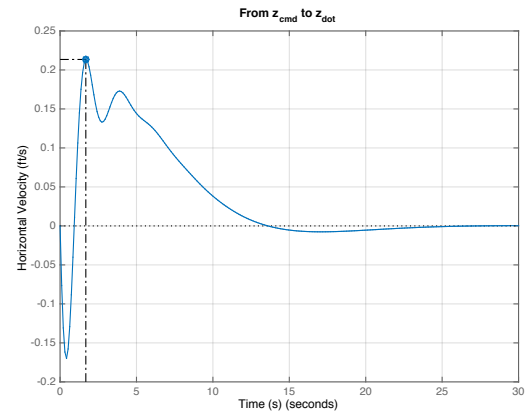**Figure 10. Step Response for Horizontal Displacement.**

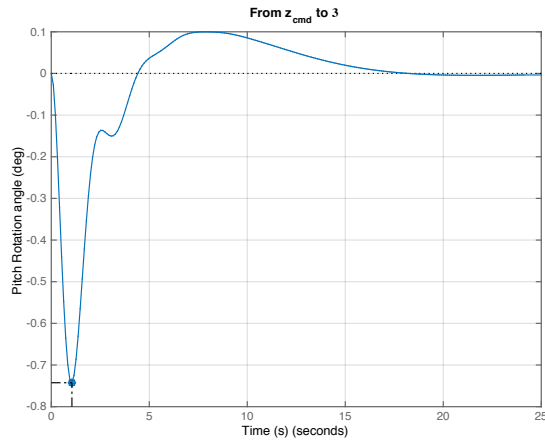**Figure 11. Step Response of Vertical Velocity.**

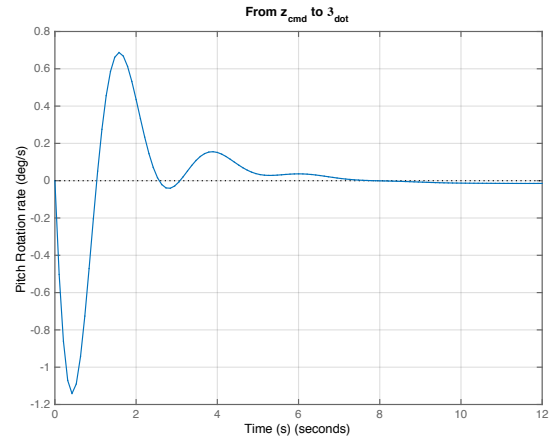**Figure 12. Step Response for Pitch Rotation Angle.**

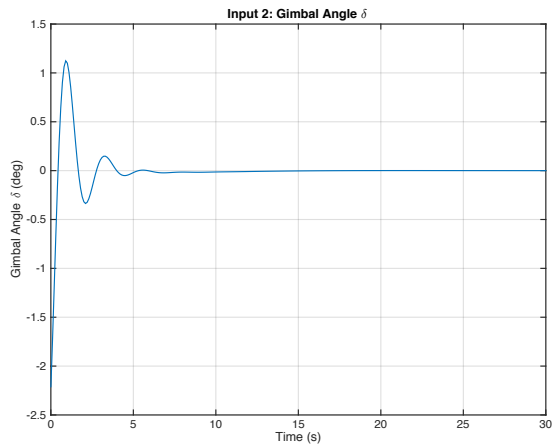**Figure 13. Step Response for Pitch Rotation Rate.**

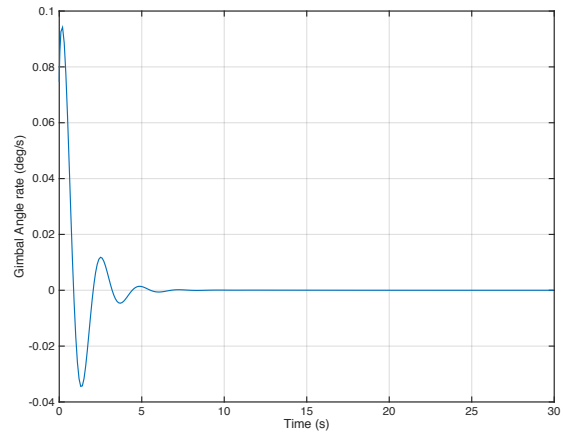**Figure 14. Input Gimbal Angle vs. Time.**

Figure 15. Input Gimbal Angle Rate vs. time.

Additional information on nominal performance is gained from the structured singular value analysis used to analyze robust performance. This information is most appropriately presented in the robust performance section.

VII.   Nominal Stability Analysis

1. Nominal Stability for Thruster Control (NS)

The closed loop poles for inner loop are listed in Table 5. The pole is negative, which indicates that the system is stable.

Table 5. Poles of Closed Loop System.

Inner closed loop poles
-5.34

2a. Nominal Stability for Gimbal Control (NS)

The closed loop poles of the final system (with all feedback loops closed) are shown in Table 6. The outermost closed loop poles all have negative real parts, which means the system is stable.

Table 6. Poles of Outermost Closed Loop System.

Closed loop poles				
Poles of closed-loop	-0.8747 + 2.6766i	-0.8747 - 2.6766i	-0.2251 + 0.2294i	-0.2251 -0.2294i

VIII.   Robust Stability Analysis

1. RS Thrust Control

Using Matlab Simulink, the bode diagram for the thrust control open loop including the designed controller was plotted in Figure 16, shown below. Recall the controller was designed to be a "stable low pass" that makes the open loop an ideal loop transfer function.
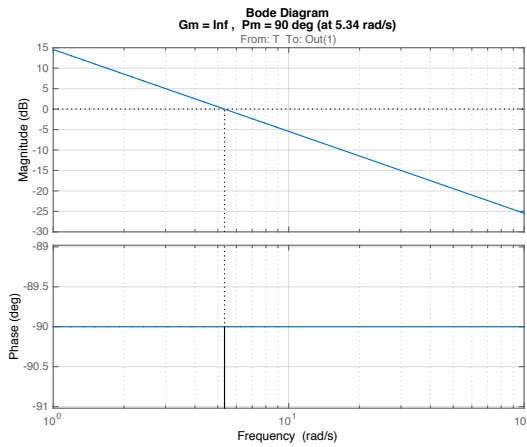

Figure 16. Bode diagram for inner open loop with designed controller.

The Bode diagram showed a good trend: high gain at low frequency (S <<1) and low gain (T <<1) at high frequency. The gain crossover frequency was 5.34 rad/s for inner open loop as expected. The inner loop has a positive infinity gain margin (GM). Also the inner loop has a 90-degree phase margin (PM). Both GM and PM satisfied standard requirements (6 dB for GM, 45 degree for PM). Also a smooth transition from low to high frequency was achieved from both inner and outer loops. The slope at crossover frequency was -20 dB/decade for both inner loop and outer loop. Both slopes are acceptable for robustness.

In order to more accurately study the robust stability of the system, the structured singular value, μ, is introduced. The definition of structured singular value is discussed in the text "Multivariable Feedback Control" by Skogestad on page 307. For clarity, we will present two forms of μ, which depend on the normalization, or lack thereof, of the uncertainty. The equations and variables corresponding to a normalized uncertainty are denoted with a "prime" or '. The first definition μ is shown in Eq. (42).

$$\mu(M)^{-1} \triangleq \{\bar{\sigma}(E)| \det(I - ME) = 0 \text{ for structured E}\}$$

$$and \; \mu(M) = \; 0 \;\; if \; no \; such \; E \; exists.$$

(42)

Note that the uncertainty, E, can be bounded by a weight and a normalized perturbation. This is shown in Eq. (43). When the weighting, w, is incorporated into the system matrix, M is modified and becomes M'. Now the definition can be restated and this is shown in Eq. (44).

$$E \leq w\Delta \quad \text{where } \overline{\sigma}(\Delta) \leq 1 \tag{43}$$

$$\mu'(M')^{-1} \triangleq \{\overline{\sigma}(\Delta)| \det(I - M'\Delta) = 0 \text{ for structured } \Delta \} \text{ where } \overline{\sigma}(\Delta) \leq 1$$

$$and \ \mu'(M') = \ 0 \ \ if \ no \ such \ \Delta \ exists. \tag{44}$$

According to the theorem, if the robust stability of a system is satisfied, $\mu'(M')$ is less than or equal to one, given appropriate weighting functions. This indicates that the weighting is sufficient; the normalized perturbation cannot destabilize the system.

The μ-analysis and the weightings correspond to multiplicative uncertainty, which seems best for dealing with the complex relationship of the uncertainty due to different trim conditions (velocity and altitude). Separate weightings were developed for the plant multiplicative uncertainty and sensor multiplicative uncertainty, shown in Eq. (49) and (50). w_I, the plant multiplicative uncertainty, was carefully chosen based on knowledge of the problem. The weighting bounds both uncertainties due to variation in the trim velocity and due to a neglected first order thrust actuator.

In order to estimate the uncertainty due to varying the trim conditions, the perturbed plant model was generated for a variety of initial altitudes and decent rates. The equations were too complex to lend themselves to an analytical evaluation of the uncertainty, so the plant was generated numerically in order to analyze the uncertainty, rather than computing a closed-form model for the plant uncertainty. Once a perturbed plant has been generated, the uncertainty is calculated using Eq. (45) and (46), shown below. Eq. (45) shows a multiplicative input uncertainty. In Eq. (46) the variable l_I denotes the uncertainty for a specific perturbed plant, whereas the previous variable w_I denotes the uncertainty bound for a set of perturbed plants. From a previous analysis, it was shown that the plant could not sustain significant variation in the trim velocity, so the weighting was selected to bound uncertainty due to a variation of 10ft/s (-290ft/s to -310ft/s). In addition to analyzing the effects of velocity changes, the effects of varying the altitude for the trim condition were briefly analyzed. They were found to be minimal and far less significant than the effects of varying the initial decent velocity. For that reason, the bounds are derived for changes due to velocity only.

$$G_p = G(I + E_I) \tag{45}$$

$$|w_I| > l_I(w) = max_{G_p \in \Pi} \frac{|G_p(jw) - G(jw)|}{|G(jw)|} \tag{46}$$

Following the velocity trim condition analysis, uncertainty due to an actuator was also considered. This is essentially neglected dynamics, and the stability of the plant was reanalyzed at the nominal trim condition of -300 ft/s. The thrust actuator break frequency was known to be approximately 5.34 rad/sec. Little more was known about the thrust actuator, so it was modeled simplistically as a first order low pass system with a unitary DC gain and variable break frequency as shown in Eq. (47). A break frequency of 4.5 rad/s or higher was selected to calculate the multiplicative uncertainty due to the actuator. Unlike the uncertainty due to the trim condition, it was relatively simple to find a closed-form expression for the uncertainty as a function of break frequency, as is shown in Eq (48).

$$A_{thruster} = \frac{b}{s + b} \tag{47}$$

$$|l_I(w)| = \left|\frac{G_p - G}{G}\right| = \left|\frac{A_{thruster}G - G}{G}\right| = |A_{thruster} - 1| = \left|-\frac{s}{s + b}\right| < |w_I| \tag{48}$$

Ultimately, a bound w_I was chosen that is shown in Eq (49). r_0, the relative uncertainty at steady state, was picked to be 0.05, and r_∞ was chosen to be 2. r_0 is commonly chosen to be 0.1 and r_∞ is typically chosen to be 2, representing 10% and 200% uncertainty respectively, as suggested in the "Multivariable Feedback Control" textbook page 274. In this case, a less conservative r_0 of 5% was selected as the analysis showed that this was sufficient for the expected uncertainty. The break frequency was chosen to be 4.55 (1/0.22) in order to bound the actuator uncertainty. Although this is slightly below the system bandwidth, the results are acceptable (shown later). The final form of w_I is shown in Eq. (49). Plots of w_I and the uncertainty described are shown in Figure 17, with uncertainty due to velocity in Figure 17 and uncertainty due to the actuator in Figure 18.

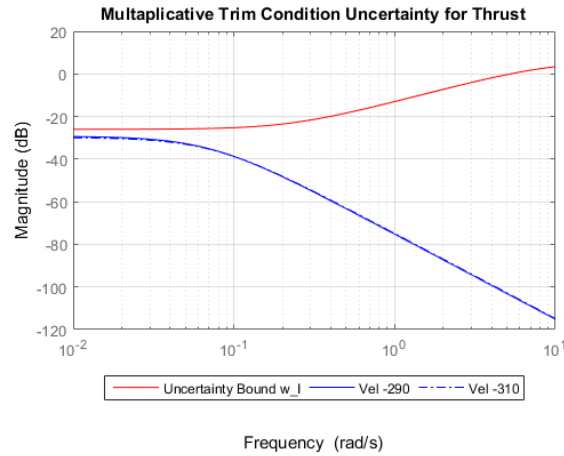$$w_I(s) = \frac{\tau s + r_0}{(\tau/r_\infty)s + 1} = \frac{0.22s + 0.05}{(0.22/2)s + 1} \tag{49}$$

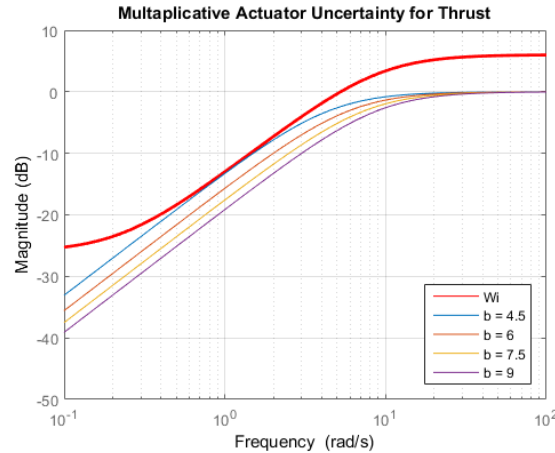**Figure 17. Thrust Velocity Uncertainty bound with w_I.**

Figure 18. Thrust Actuator Uncertainty bound with w_I.

The multiplicative uncertainty of the sensors, w_s, was chosen less precisely than that of the multiplicative input uncertainty. The focus of the project was on estimating the uncertainty of the plant, so a conservative uncertainty bound was simply chosen for the sensors that satisfied engineering judgement. The standard r_0 and r_∞ values of 0.1 and 2 were used, and a bandwidth of 1000 rad/s was deemed reasonably conservative. This was based on knowledge that high quality sensors often have bandwidths in the range of several hundred Hz, and 1000 rad/s is approximately 160Hz. The form of the sensor uncertainty is shown in Eq. (50).

$$w_s(s) = \frac{\tau s + r_0}{(\tau/r_\infty)s + 1} = \frac{0.001s + 0.1}{(0.001/2)s + 1} \tag{50}$$

After finalizing the uncertainty weightings, μ-analysis was used to analyze robust stability. Table 7 summarizes the structured singular value for different loop combinations. Loop RS w_I corresponds to the loop from $w2$ to $z2$ in Figure 18 (the RS associated with only a multiplicative input uncertainty). Loop RS w_s corresponds to the loop from $w3$ to $z3$ (the RS associated with only uncertainty in the sensor feedback), and loop RS combined corresponds to the combination of loop u and loop y. The structured singular values were calculated using the Matlab function *mussv*. The structured singular values for actuator and sensor multiplicative perturbations are also plotted against frequency in Figure 19. As can be seen in the table and the figure, robust stability is satisfied. Furthermore, the appropriate relationships between individual robust stability and combined robust stability are also satisfied.

Table 7. Structured Singular Value Analysis for actuator and sensor perturbations.

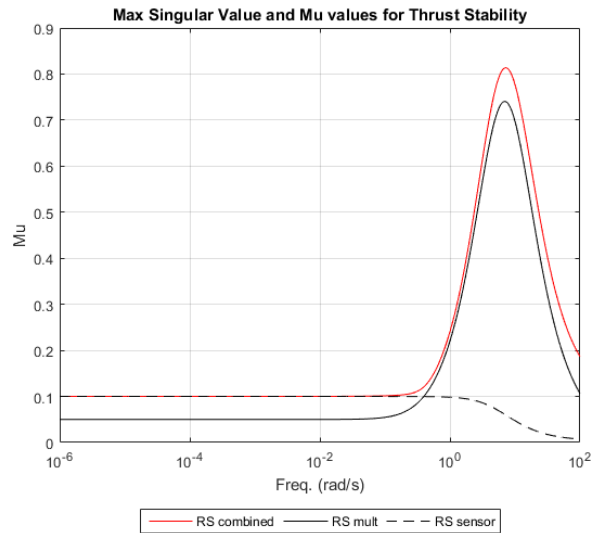| Loop	Frequency (rad/s)	Max(μ)
RS w_I	7.01	0.74
RS w_s	0.00	0.10
RS combined	7.27	0.81

Figure 19. Robust Stability Results for Various Channels.

2. RS Gimbal Control

Similar to the thrust control analysis, the single-loop-at-a-time technique was used as a preliminary analysis of robust stability for gimbal control. The Bode-diagram of each open-loop with the designed controller is shown in Figure 20, 21, 22, and 23. In Figure 20, the Bode diagram of $z4$ to $w4$ has a gain crossover frequency of 0.2 rad/s. Its gain margin is 15.3dB and phase margin is 61.3 deg. Those margins were deemed to be acceptable. The closed-loop system has high gain at low frequency and low gain at high gain frequency, which implies good reference tracking and noise rejection. In Figure 21 the Bode diagram of input $z3$ to $w3$ has a GM of 3.52 dB and PM of 67.52 degrees. The GM was below the standard requirement by 2.4 dB, but this is attributed to the difficult pole-zero dynamics of the plant. In Figure 22, the Bode diagram of $z2$ to $w2$ has a lower GM of -9.6427 dB and an upper GM of Inf dB. Two PM are -55.93 and 27.35 degrees. Those margins do not satisfy the standard requirements; this means the plant is sensitive to modeling uncertainties or perturbations that directly affect θ. This should be improved in the future

through the use of robust control tools. Finally, in Figure 23 the Bode diagram of z_1 to w_1 has a lower GM of -3.703 dB and an upper GM of 22.06 dB. Two PM are -38.33 and 53 degrees. Similarly, those margins are not robust; a better controller should be designed if time is permissible. It should also be noted that these gain and phase margins represent perturbations to individual channels or loops. They are best-case scenario bounds, and simultaneous perturbations could have very negative effects on the plant, which will be investigated using a μ-analysis. Table 8 shows a summary of the GM and PM, as well as the corresponding frequencies.
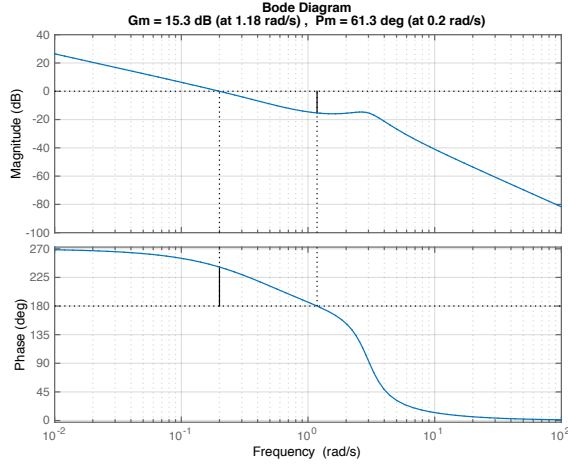

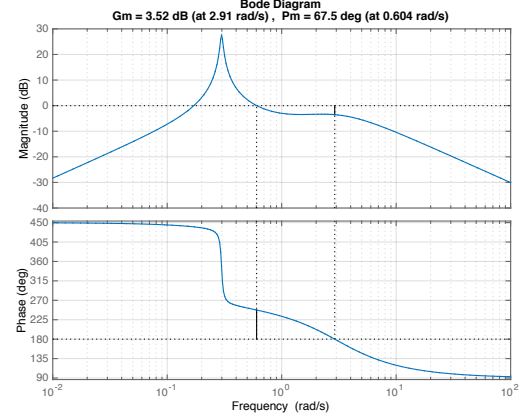**Figure 20. Open Loop Bode Diagram from input z_4 to output w_4.**

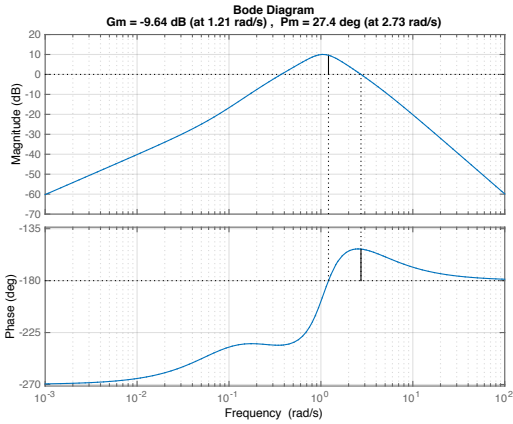**Figure 21. Open Loop Bode Diagram from input z_3 to output w_3.**

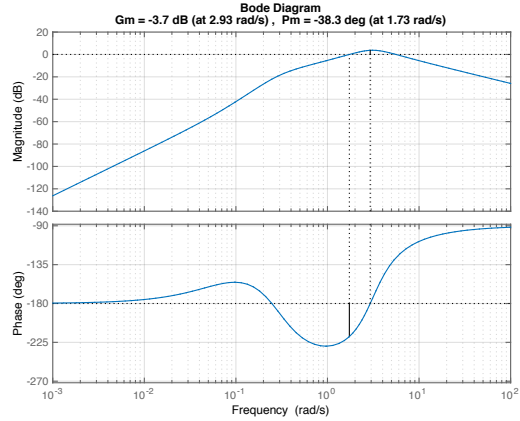**Figure 22. Open Loop Bode Diagram input z_2 to output w_2.**

Figure 23. Open Loop Bode Diagram input z_1 to output w_1.

Table 8. Open loop system's GM and PM.

	GM(dB)		GM Freq (rad/s)		PM(degree)		PM Freq (rad/s)	
Input z_4 to output w_4	15.3466		1.1789		61.3040		0.2000	
Input z_3 to output w_3	3.5226		2.9069		-99.8471	67.5218	0.1710	0.6040
Input z_2 to output w_2	-9.6427	Inf	1.2089	Inf	-55.9370	27.3536	0.3690	2.7280
Input z_1 to output w_1	-3.7038	22.0602	2.9284	0.2470	-38.3297	53.0035	1.7332	5.5961

In order to develop more accurate bounds on robust stability, a μ-analysis was carried out using the same technique described previously. The μ-analysis was done for uncertainty only in the actuator channel, uncertainty in

all of the feedback channels but not the actuator channel, and uncertainty in all of the feedback channels as well as the actuator channel simultaneously.

Similar to the thrust plant, weightings were also developed for multiplicative input uncertainty and multiplicative sensor uncertainty. It should be noted that, for the thrust control plant, the output has one uncertainty l_I because the system is SISO. The gimbal control plant has multiple outputs for a single input (SIMO), and each output (4 outputs total) has a corresponding uncertainty l_I. Ultimately, one upper bound, w_I, is chosen such that each output uncertainty, l_I, is bounded. Considering the sensor feedback channels, each channel is a scalar and has a separate weighting. For simplicity, as well as the reasons mentioned previously, the same weighting was used for the sensors in the gimbal plant as in the thrust plant. The sensor weighting, w_s, is repeated in Eq (51).

$$w_s(s) = \frac{\tau s + r_0}{(\tau/r_\infty)s + 1} = \frac{0.001s + 0.1}{(0.001/2)s + 1} \tag{51}$$

The multiplicative input uncertainty weight, w_I, for the gimbal plant was developed shown in Eq. (54) using the method previously described in the RS Thrust Control section. The uncertainty was analyzed numerically for a variation in trim condition velocity of 10 ft/s (-290ft/s to -310ft/s). The low frequency relative uncertainty was determined by the uncertainty for this velocity variation in the z and zdot channels. It was found to be far more significant than the uncertainty in the thrust control case, yielding a value of 28% (as opposed to 5% for the thrust control case).

The multiplicative uncertainty also had to bound the uncertainty from the neglected dynamics of a second order gimbal actuator. The break frequency of the gimbal actuator was known to be approximately 30 rad/sec. Because the actuator is controlling the position of a physical system with mass, a second order transfer function was chosen to represent the system. This 2nd order actuator form is shown in Eq. (52). For simplicity, the system is assumed to have a natural frequency of 30 rad/sec, although the damping ratio and DC gain are treated as variable parameters. Eq. (53) shows how the multiplicative input uncertainty is calculated for this actuator.

$$A_{gimbal} = DC \frac{w_n{}^2}{s^2 + 2\zeta w_n s + w_n{}^2} \tag{52}$$

$$|l_I(w)| = \left|\frac{G_p - G}{G}\right| = \left|\frac{A_{gimbal}G - G}{G}\right| = \left|A_{gimbal} - 1\right| < |w_I| \tag{53}$$

In an effort to create a reasonably conservative bound, the DC gain was allowed to vary from 0.75 to 1.25 and the damping ratio ζ was allowed to vary from from 0.5 to 1.5. Multiplicative uncertainty was generated for a series of combinations of these parameters, and w_I was shaped accordingly. The uncertainty due to the actuator determined the frequency properties and the high frequency gain of the bound. This led to a high frequency relative uncertainty of 200% and a crossover frequency near 10 rad/s (1/0.1). The final form of the multiplicative input uncertainty w_I is shown in Eq (54).

$$w_I(s) = \frac{\tau s + r_0}{(\tau/r_\infty)s + 1} = \frac{0.1s + 0.28}{(0.1/2)s + 1} \tag{54}$$

Plots of the bound w_I and the uncertainties described are shown in Figures (24) and (25). The uncertainty due to velocity changes is in Figure 24 and the uncertainty due to the neglected actuator is shown in Figure 25. It can be seen that the bound satisfies the uncertainty expected in the plant. This is a very conservative bound, as this plant is strongly affected by the uncertainties present.
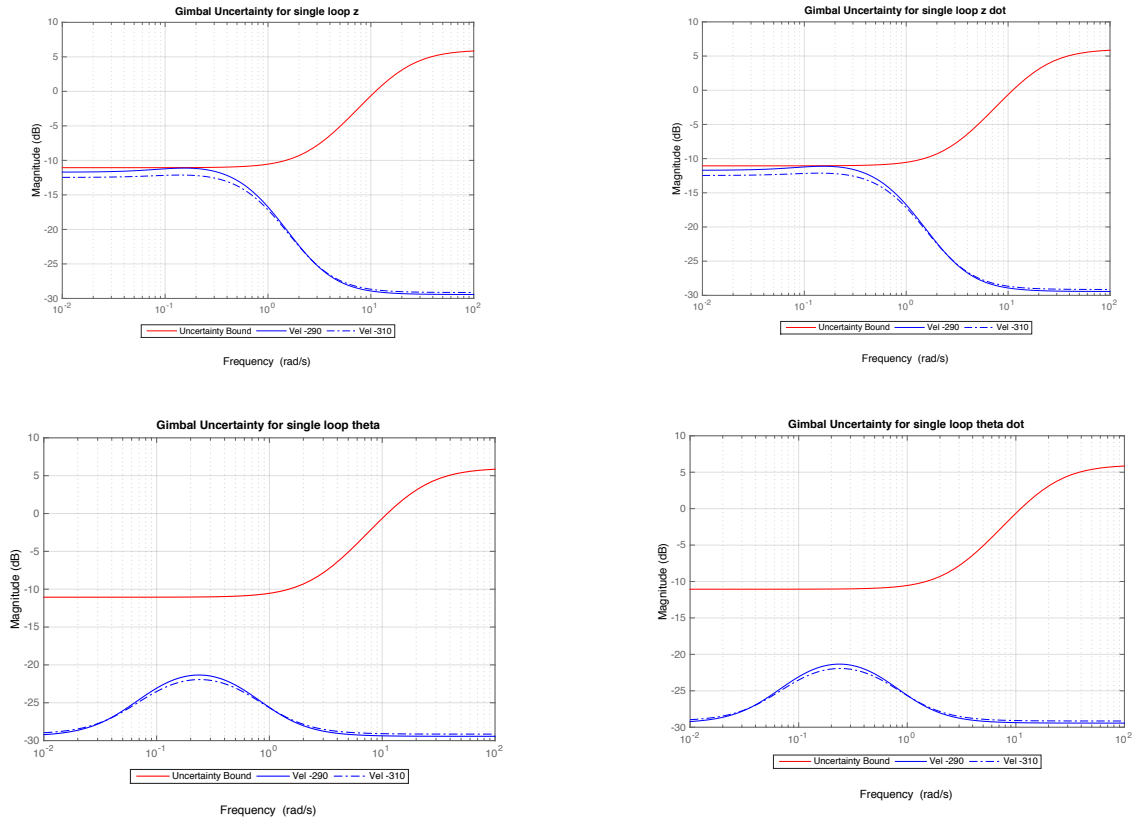
Figure 24. Gimbal Uncertainty for single loop for z, $\dot{z}, \theta$ and $\dot{\theta}$.
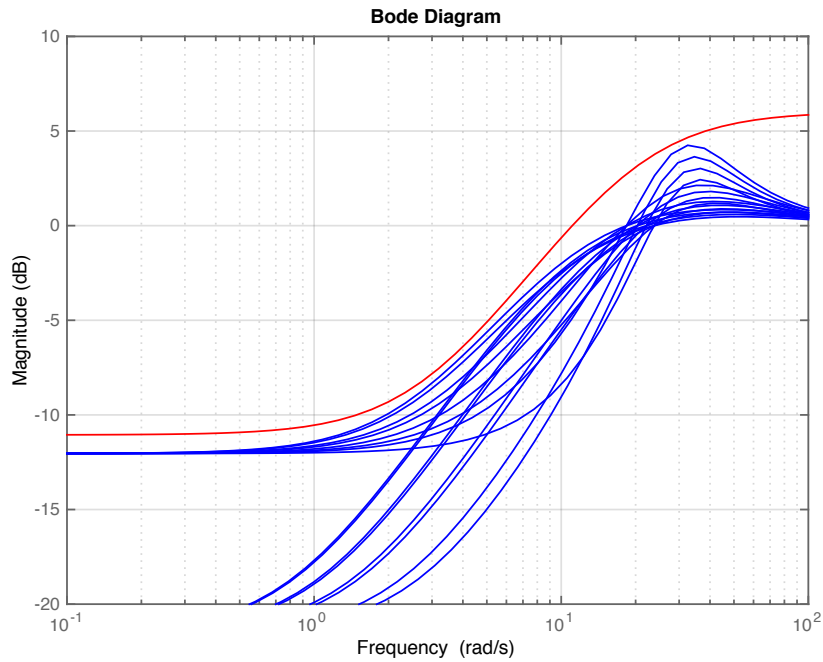

Figure 25. Different 2ⁿᵈ order Actuators with single and multiple loop 1/μ upper bound.

American Institute of Aeronautics and Astronautics

The results of the maximum singular value and the μ-analysis are shown in Figure 26 and tabulated in table 9. The μ value increases as the number of channels considered increases, as is expected. It should be noted that this plant has larger μ values than the thrust control plant, and is therefore less robust. This is expected due to the unstable pole and zero in the open loop plant, as well as the highly conservative multiplicative input uncertainty bound. Looking at the values in Table 9, maximum singular value for implicative input uncertainty (actuator) and implicative output certainty (sensors) are less than 1 respectively. However, the maximum singular value of the combined RS was greater than 1, therefore RS is not satisfied for combined uncertainty. From the plot, it can be observed that both the plant uncertainty and the sensor uncertainty contribute significantly to the failing of robust stability. In order to find out which sensor channel contributes most significantly to the high μ value, Figure 27 was generated to compare the structured singular value for robust stability of the individual sensors. One can see that the $\dot{\theta}$ sensor contributed the most for maximum singular value, and the only sensor error that appears relatively insignificant is the $\dot{z}$ sensor.
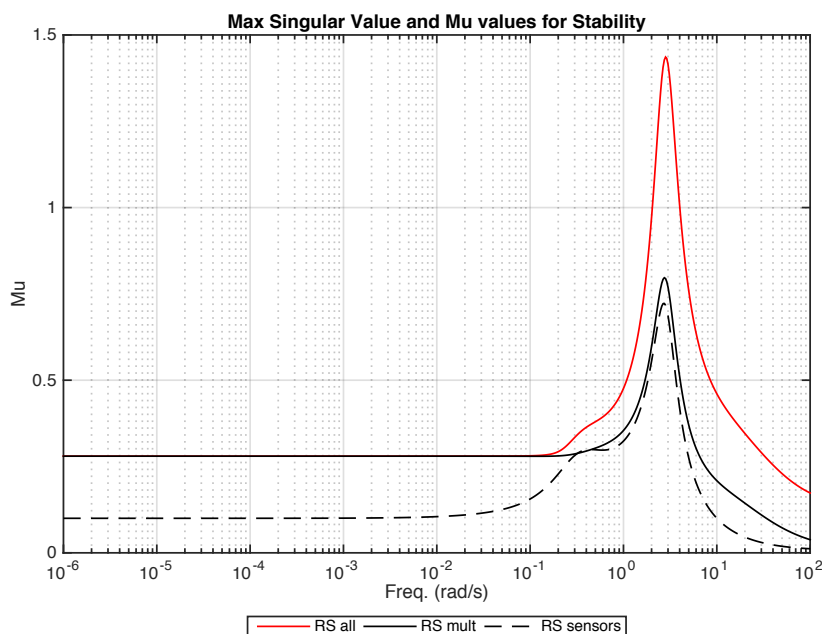

Figure 26. Structured singular value for actuator and sensor perturbations (RS).

Table 9. Structured Singular Value Analysis for actuator and sensor perturbations

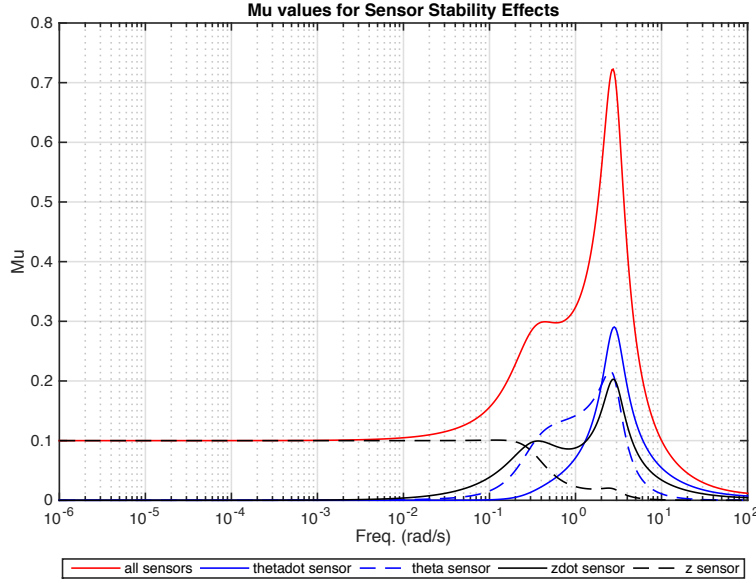| Loop	Frquency (rad/s)	Max(μ)
RS w_I	2.7378	0.72
RS w_s	2.7378	0.80
RS combined	2.8233	1.44

Figure 27. Structured singular value for Sensor Stability effects.

When considering uncertainty in the sensor feedbacks, it should be noted that the μ value is much higher for the gimbal control system than the thrust control system. Both plants will experience the same change in trim condition, so the less robust plant will impose restrictions on both plants. The lack of robustness in the gimbal control plant will ultimately limit the variation in descent speed, despite the robust properties of the thrust control plant.

IX. Robust Performance Analysis

1. RP Thrust Control

In order to analyze robust performance, a robust stability problem was posed with a fictitious disturbance representing a loop closure from the tracking error to the disturbance input. If robust stability is satisfied with the fictitious uncertainty, then robust performance can be concluded. For a weighted analysis, the performance weighting w_p would be used for the uncertainty weighting. The relationship necessary for robust performance is shown in Eq. (24) in the early section.

Using the information provided in Eq. (24) and an appropriate system bandwidth, the desired sensitivity function is chosen and bound by Eq. (55) for thrust control. The low frequency and high frequency values are standard for performance specifications, and the bandwidth is chosen to be slightly less than the open loop crossover frequency of the thrust plant (5.34 rad/s).

$$w_P(s) = \left(\frac{\frac{s}{M^{1/n}} + w^*_B}{s + w^*_B A^{1/n}} \right)^n = \frac{\frac{s}{2} + 4.5}{s + 4.5(0.0001)} \tag{55}$$

The inequality in Eq. (25) can provide a criterion for either nominal or robust performance. If no uncertainties (no w_I) are considered besides the fictitious performance loop uncertainty, then the analysis applies to nominal performance. The maximum singular value of the loop transfer function (from the fictitious input to the weighted output) indicates whether the performance bound is satisfied for a nominal plant. Conversely, if actual uncertainties (as described in robust stability) are included in the analysis, a μ-analysis result indicates whether the performance

bound is satisfied for the entire set of perturbed plants, which is robust performance. In Table 10, the letter u indicates the fictitious uncertainty in the performance loop, and the letter y indicates the actual expected uncertainty in the plant. The relationship between NP, RS, and RP is summarized in Table 10. Structure singular values were plotted for NP, RS, and NP respectively in Figure 28. The maximum μ over all frequencies is listed in Table 11.
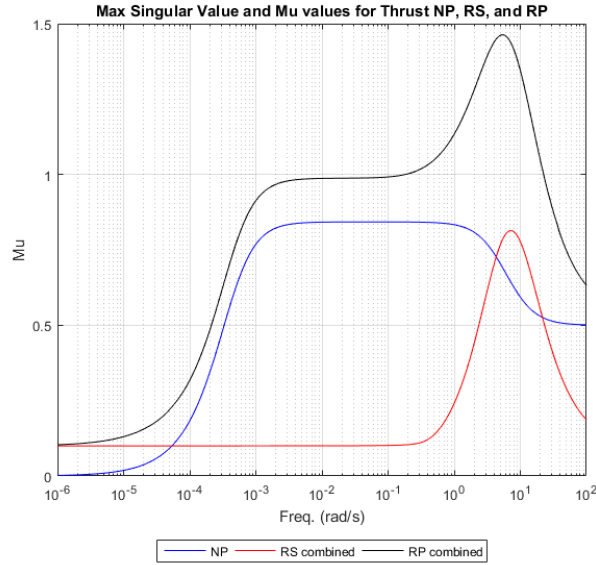

Figure 28.Thruster Control Structure Singular Value for NP, RS and RP respectively.

Table 10. Relationship between tabs in Thruster Simulink and corresponding meanings.

u	$\dot{x}$ Disturbance (tab 3)	NP	
y	z1 to w1 (Tab 1) RS1	RS	RP
	z2 to w2 (Tab 2) RS2		

Table 11. Max Singular Value and Structured Singular Value Analysis for NP, RS, RP.

Loop	Frequency (rad/s)	
u (NP)	0.0551	0.84 Max(σ)
y (RS)	6.4509	0.81 Max(μ)
uy (RP)	5.0281	1.46 Max(μ)

Table 11 shows that NP and RS were satisfied, but RP was not satisfied. This was probably due to a tight weighting on both w_I and w_s in the RS stability section. In Figure 28, the inverse of the nominal performance and robust performance inverse μ values were plotted with the performance bound from Eq. (55).

2. RP Gimbal Control

Similar to the thrust control, nominal and robust performance of the gimbal control were analyzed using μ-analysis. For the gimbal control, a slightly different performance weighting was chosen and is shown in Eq. (56).

$$w_P(s) = \left(\frac{\frac{s}{M^{1/n}} + w^*{}_B}{s + w^*{}_B A^{1/n}} \right)^n = \frac{\frac{s}{2} + 0.1}{s + 0.1(0.0001)} \tag{56}$$

The variables that determine NP, RS, and RP are summarized in Table 12. Note that the fictitious uncertainty now enters into four channels, rather than one, as this system is SIMO. However only a z disturbance was considered because it is the main variable to be control (e.g. landing on the barge requires precise horizontal placement). The resulting singular values are plotted and summarized in Figure 29 and Table 13 respectively. It can be seen that the μ values for the gimbal controller are much more restrictive than those for the thrust controller. This is expected due to the additional channels and the increased difficulty of the underlying dynamics. Nominal performance was satisfied, but robust stability, and consequently robust performance, were not satisfied for the gimbal control system.

From Figure 29, it can be observed that robust stability drives up the peak of robust performance. This indicates that robust performance cannot be improved without improving robust stability. There is a secondary peak that is much smaller but still great than one (around 0.3 rad/s). This peak appears to be strongly influenced by nominal performance, indicating that NP must improve in addition to RS in order to improve RP.

Table 12 Relationship between tabs in Gimbal Simulink and corresponding meanings.

u	$\dot{z}_a$ Disturbance (tab 1)	NP	
	z6 to w6 (Tab 2)		
	z1 to w1 (Tab 3)		
y	z2 to w2 (Tab 4)	RS	RP
	z3 to w3 (Tab 5)		
	z4 to w4 (Tab 6)		

Table 13. Structured Singular Value Analysis.

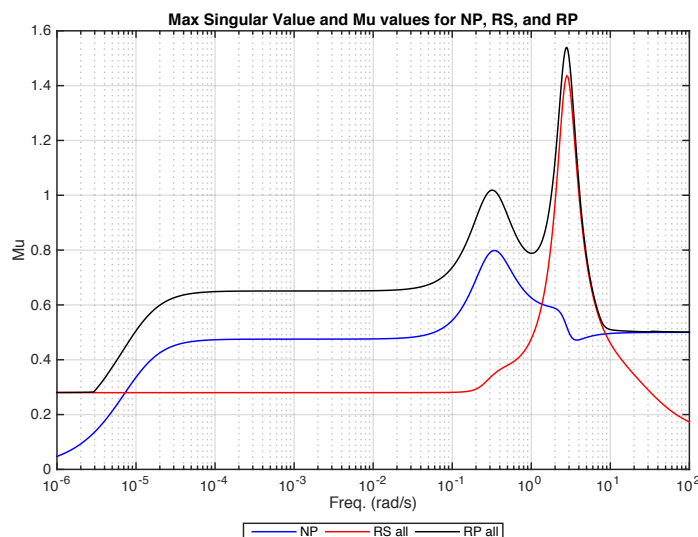| Loop	Frequency (rad/s)	
u (NP)	0.3382	0.80 Max(σ)
y (RS)	2.8233	1.44 Max(μ)
uy (RP)	2.8233	1.54 Max(μ)

Figure 29. Gimbal Control Structured Singular Value for NP, RS, RP respectively.

In order to see which channel most significantly affects RP, Figure 30 and 31 were generated. Figure 30 shows μ values for RP due to only the plant uncertainty and only the combined sensor uncertainty. Furthermore, Figure 31 shows each individual RP μ value for the different sensors, and it reveals how each sensor affects the combined sensor RP. From Figure 30, one can see that sensors contributed more uncertainty than input multiplicative

uncertainty (actuators) as expected. From Figure 31, all of the sensors are noted to be important contributors to the degradation of robust performance. It is determined, however, that uncertainty in the horizontal displacement sensor has the most negative affect on RP. For a full analysis in the future, more detailed specifications should be found for the different sensors to be used, leading to unique weightings and a more accurate idea of which sensor most negatively affects the performance of the system.
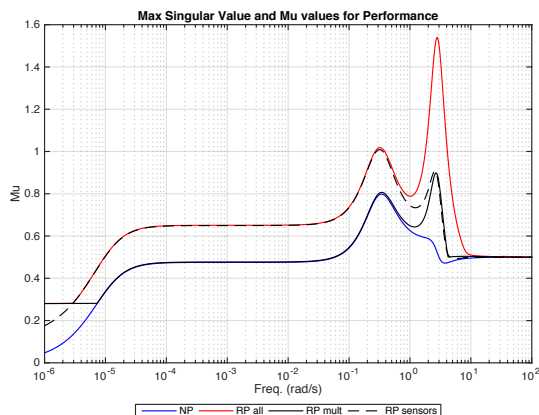

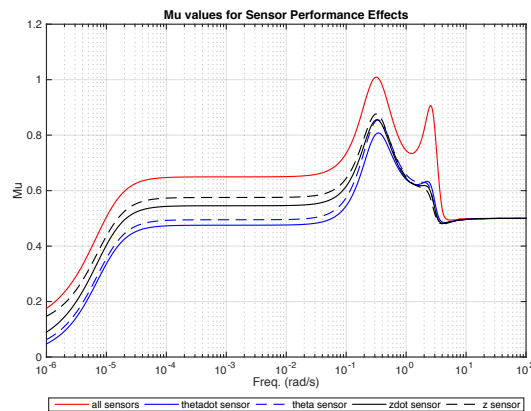**Figure 30. Structured Singular Value for different Performance.**

Figure 31. Structured Singular Value for Performance at different sensors.

X.   Conclusion

This project pertains to stability and control of an inverted rocket landing. It spans the modeling of the rocket, the control design, and a detailed stability, performance, and robustness analysis. The nonlinear equations governing the rocket motion were linearized about a chosen flight condition to create an LTI multivariable model. The model decoupled into two subsystems, thrust control (SISO) and gimbal control (SIMO). A straightforward single loop controller was designed for the stable low pass thrust control system. A more complex, nested controller was designed for the gimbal control system, which was approximated to be a chain of integrators. Both designs satisfied nominal stability. The time domain response characteristics were acceptable for both nominal systems as well. Nominal performance was satisfied for the thrust controller and for a z disturbance in the gimbal controller. Robust stability single-loop-at-a-time and structured-singular value analyses revealed that the thrust control system is reasonably stable but that the gimbal control system has small tolerances for uncertainty. This was expected due to the difficult dynamics inherent to the plant. For a detailed NP, RS, and RP analysis, uncertainty weightings were chosen to bound multiplicative input uncertainty due to changes in the velocity trim condition as well as neglected actuator dynamics. Furthermore, uncertainty was also considered in all the feedback channels, and appropriate weightings were derived. Through performance weightings, it was revealed that both plants are able to satisfy nominal performance. Furthermore, the thrust plant satisfies robust stability, but the gimbal plant fails to do so. Neither plant successfully satisfied robust performance when considering uncertainty in all possible channels, but the highest structured-singular-value overall was 1.54. Although this fails the robust performance criterion, this is considered successful for a first iteration. The outlook for designing a satisfactorily robust controller is therefore optimistic.

Appendix

Matlab code is very long, but it is available upon request.

References

[1]Enn, Dale, *Guidance & Control For DC-X Hover & Translate Flights*, Honeywell, March 9, 1993.
[2]Skogestad, Sigurd, *Multivariable Feedback Control Analysis and Design*, 2nd edition, John Wiley, 2005.